PAPER

Check for updates

Porosity evolution and oxide formation in bulk nanoporous copper dealloyed from a copper–manganese alloy studied by *in situ* resistometry†

Elisabeth Hengge, [ID] *[a] Jakob Ihrenberger,[a] Eva-Maria Steyskal [ID] [a]
Ricardo Buzolin, [ID] [bc] Martin Luckabauer, [ID] [d] Christof Sommitsch [ID] [b]
and Roland Würschum [ID] [a]

The synthesis of bulk nanoporous copper (npCu) from a copper–manganese alloy by electrochemical dealloying and free corrosion as well as the electrochemical behaviour of the dealloyed structures is investigated by *in situ* resistometry. In comparison to the well-established nanoporous gold (npAu) system, npCu shows strongly suppressed reordering processes in the porous structure (behind the etch front), which can be attributed to pronounced manganese oxide formation. Characteristic variations with the electrolyte concentration and potential applied for dealloying could be observed. Cyclic voltammetry was used to clarify the electrochemical behaviour of npCu. Oxide formation is further investigated by SEM and EDX revealing a hybrid composite of copper and manganese oxide on the surface of a metallic copper skeleton. Platelet-like structures embedded in the porous structure are identified which are rich in manganese oxide after prolonged dealloying. As an outlook, this unique heterogeneous structure with a large surface area and the inherent properties of manganese and copper oxides may offer application potential for the development of electrodes for energy storage and catalysis.

1 Introduction

Porous metals are promising materials in many fields of application including (bio-)catalysis,[1,2] energy storage[3–5] and sensing.[6,7] In particular, nanoporous metal electrodes prepared by selective etching, so-called (electrochemical) dealloying, are highly interesting due to their free-standing structure, high surface-to-volume ratio and thermal as well as electrical conductivity. By far the best known nanoporous metal is nanoporous gold (npAu), but also other noble metals such as nanoporous platinum (npPt), palladium (npPd) or silver (npAg) have been investigated extensively.[7–9] For future application, nanoporous metals based on noble metal alloys might not be suitable because of their high costs and environmental impact. Hence, non-precious metals have gained increasing interest, among which is nanoporous copper (npCu). Nanoporous

copper electrodes exhibit a variety of potential applications in green and sustainable chemistry, *e.g.* as anode materials for lithium-ion batteries,[10–12] as catalysts[13–15] and for sensors.[16] In the literature, synthesis of npCu from AlCu,[16–20] SnCu,[11] TiCu,[21] CeCu,[22] NiCu,[17] ZnCu[17,23,24] and CuMn[25–27] has been reported, whereby the resulting nanoporous structures differ greatly depending on experimental parameters and alloy composition. Among them, nanoporous copper from copper–manganese gained a lot of interest as it exhibits one of the largest differences in electrochemical potential (difference of 1.477 V between Mn/Mn^{2+} and Cu/Cu^{2+})[28] from the alloys mentioned above. This characteristic feature is essential for successful electrochemical dealloying. Furthermore, a single phase alloy can be obtained.

Up to now, only a few studies are available which focus on the systematic understanding of the dealloying of this alloy system. Early investigations on the dealloying process and the porous structure of copper manganese alloys started in the 1980s,[29–31] but studies on microstructural composition of the porous structure[32,33] or electrocatalytic performance[13,25] have been performed only in recent years. Also, strong influence of the pH-value and concentration[26,28,34] of the electrolyte as well as of previous heat treatment[35] has been reported. The high chemical reactivity of both copper and manganese makes the (electro-)chemistry of these systems highly complex. For example, pronounced oxide formation of both alloy components has been reported[25,32] but a full understanding of the

[a]Institute of Materials Physics, Graz University of Technology, Petersgasse 16, A-8010 Graz, Austria. E-mail: e.hengge@tugraz.at; Tel: +43 316 873-8481

[b]Institute of Materials Science, Joining and Forming, Graz University of Technology, Kopernikusgasse 24, A-8010 Graz, Austria

[c]Christian Doppler Laboratory for Design of High-Performance Alloys by Thermomechanical Processing, Kopernikusgasse 24, 8010 Graz, Austria

[d]Department of Mechanics of Solids, Surfaces and Systems, Faculty of Engineering Technology, University of Twente, Drienerlolaan 5, 7522NB Enschede, The Netherlands

† Electronic supplementary information (ESI) available. See DOI: https://doi.org/10.1039/d2na00618a

underlying kinetics is still missing. At the same time, deliberate control of oxide formation is of great importance for many applications including energy storage and sensing.[14,25,25,36]

Studies of the dealloying and the electrochemical performance of dealloyed npCu will significantly contribute to the fundamental understanding of the structural evolution. There are several methods for investigating dealloying processes (including X-ray scattering,[37–39] X-ray diffraction,[40] and electron microscopy[41,42]), but most methods are surface specific and focus on small volumes. One method, which is particularly well suited to investigate the dealloying process on a larger scale is *in situ* resistometry[43] which enables the monitoring of the entire sample and the study of the evolution of the porous structure in real time. This method has been recently applied by our group for studying npPt,[43,44] npPd,[45] and npAu.[44,46]

The present work aims at a comprehensive investigation of npCu using *in situ* resistometry to analyse the structural evolution during electrochemical dealloying as well as the electrochemistry of the dealloyed state. The findings are compared to data obtained by scanning electron microscopy (SEM) and energy-dispersive X-ray spectroscopy (EDS). Potential-controlled dealloying in different electrolytes and varying potentials is compared to free corrosion (chemical dealloying). *In situ* resistometry shows that oxide formation strongly influences the surface diffusivity. The formation of manganese oxide incorporated in the porous structure as a result of prolonged dealloying is identified. The findings significantly contribute to the understanding of the dealloying mechanisms as well as electrochemical performance of CuMn alloys. Potential future application fields include energy storage and catalysis.

2 Materials and methods

2.1 Electrochemical dealloying and characterization

The master alloy for dealloying was prepared following the preparation routine described by Hayes *et al.*[26] The alloy composition was evaluated using X-ray diffraction (XRD) and energy dispersive X-ray spectroscopy (EDS), revealing an fcc structure with a final composition of 68 at% Mn and 32 at% Cu. The XRD spectrum is shown in Fig. SI-1 in the ESI.†

The master alloy was cut into small sample pieces (approx. $10 \times 12 \times 0.7$) mm with an average weight of 120 mg) using a high precision saw. Directly before each measurement, the respective sample was ground with a piece of SiC paper to remove any oxide layer formed during cutting and storage. After rinsing with ethanol, the sample was then wrapped with copper wires for electrical contact. All electrochemical measurements were performed in a three electrode setup with concomitant *in situ* resistometry. A schematic representation of the setup is shown in Fig. 1. Commercial Ag/AgCl (saturated KCl) was used as the reference electrode; a Pt-wire and a carbon cloth was used as the counter electrode for electrochemical dealloying and cyclic voltammetry, respectively. Each CuMn sample was made to come in contact with five wires, the middle one serving as the working electrode, the outer wires enabling a four point resistance measurement. Thereby, the two outermost wires were
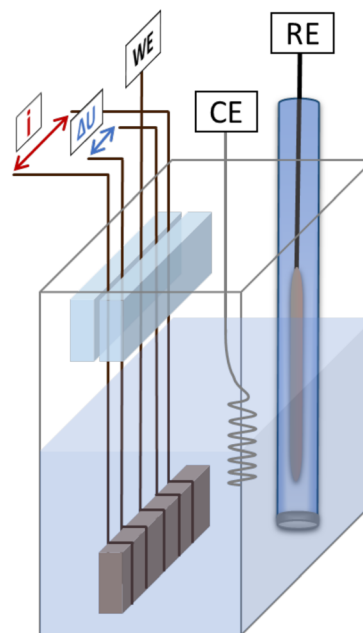

Fig. 1 Schematic representation of the setup used for electrochemical dealloying with complementary *in situ* resistometry. The sample is made to come in contact with five Cu-wires, the middle one representing the working electrode (WE), and the outer four are used for applying current pulses (*i*) and measuring the potential drop (ΔU) for the four-point resistance measurement. RE and CE represent the reference and counter electrode, respectively.

used for applying the current (100 mA pulses) and the inner two wires, for measuring the potential drop. Any influence of *in situ* resistometry on the electrochemical measurements was excluded in previous studies.[44] To ensure that no mechanical stress was applied to the sample through the wires, the wires were mounted between two acrylic glass pieces which were glued together with a two-component adhesive. This mechanical fixation was placed well above the fluid surface to avoid any contact with the electrolyte (for details see Fig. 1). The electrochemical measurements were performed using an Autolab PGSTAT204 potentiostat, and the resistance change was monitored with a Keithley 2400 Source Meter. Solutions of 0.1 and 0.04 M HCl (diluted from 1 M HCl in high purity water) were used as electrolytes for dealloying based on the results presented by Wang *et al.*[47] 0.1 M KOH (prepared by dissolving an appropriate amount of KOH platelets (≥85% in high purity water) was used as the electrolyte for cyclic voltammetry. All chemicals were purchased from Carl Roth.

After dealloying, the electrochemical cell (including the sample) was immersed in distilled water. Subsequently, cyclic voltammograms (CV) were recorded in 0.1 M KOH and again monitored by *in situ* resistometry.

2.2 Scanning electron microscopy

For scanning electron microscopy (SEM) and energy dispersive X-ray spectroscopy (EDS), three additional samples were prepared following the same routine as described above

(including dealloying and cycling in 0.1 M KOH), ensuring similar sample size and weights. After thoroughly rinsing with water and ethanol and subsequent drying, the samples were cut in half using a scalpel and mounted on the SEM sample holder. The SEM images and EDS spectra were recorded from the cross section of the sample. For microstructural analysis, the SEM images were analysed with ImageJ open source software.[48]

The studies were performed using a TESCAN Mira3 electron scanning microscope equipped with an energy dispersive X-ray (EDS) Octane Super A spectrometer. Backscattered (BSE) and secondary electron (SE) micrographs were acquired using an acceleration voltage of 3 kV and 15 kV and a beam spot size between 2 nm and 30 nm. The working distance varied between 2 mm and 15 mm. EDS analysis was performed at an acceleration voltage of 15 kV with a beam spot size of 30 nm and a working distance of 15 mm. The chemical composition reported here is semi-quantitative as no calibrant was used for the analysis.

For determination of the overall elemental composition of dealloyed npCu, one sample was further analysed by X-ray fluorescence spectroscopy using a Panalytical Epsilon 1 XRF analyzer equipped with an Ag anode.

3 Results

3.1 Dealloying

To examine the influence of the potential and electrolyte concentration, dealloying was performed in 0.1 M HCl at −300 mV (sample R-1) and −500 mV (sample R-2) as well as in 0.04 M HCl at −300 mV (sample R-3). Prior to the dealloying experiments, a polarization curve (see Fig. SI-2 in the ESI†) was recorded with a separate CuMn sample to ensure proper choice of dealloying potential. One sample was dealloyed under free corrosion conditions in 0.1 M HCl (sample R-F). A list of the samples including the dealloying conditions is shown in Table 1.

In Fig. 2 the current *vs.* time evolution (a) as well as the relative change in electrical resistance (b) during electrochemical dealloying is shown (samples R-1, R-2 and R-3). For better comparison and to account for the different sample sizes, the current is normalized by using the macroscopic surface area A_{macro} of each sample which is determined from the outer dimension of the CuMn sample. The values for A_{macro} are also given in Table 1.

The time evolution of the current density in Fig. 2(a) shows characteristics known from other dealloying experiments,[43]
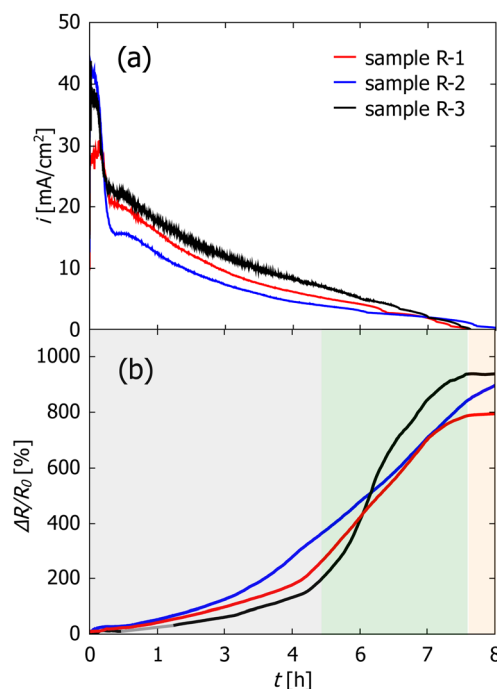

Fig. 2 Current density in mA cm^{-2} (a) and change in relative electrical resistance $\Delta R/R_0$ in % (b) during potential-controlled dealloying. Sample R-1 was dealloyed in 0.1 M HCl at −300 mV (red), sample R-2 in 0.1 M HCl at −500 mV (blue) and sample R-3 in 0.04 M HCl at −300 mV (black). The background colors mark the different regimes in the dealloying process as discussed in the main text.

starting at rather high currents followed by a steep decrease which is caused in this system by the depletion of Mn atoms on the surface. The decrease in current density is followed by a short period of constant current and a subsequent slow decrease which lasts up to 7–8 h of total etching time. This is then interrupted by a kink in current. Afterwards, the current stays nearly constant at slightly negative values (in the range of −10 to −100 μA cm^{-2}).

The relative change $\Delta R/R_0$ in resistance in Fig. 2(b) can be divided into three regimes, which are marked by the different background colors. First the resistance increase is rather slow with a nearly linear increase up to 4 to 5 h hours of dealloying. Then, the resistance starts to increase very fast resulting in a resistance increase of three orders of magnitude. Finally, in the third regime which starts simultaneously with the current

Table 1 List of samples used for dealloying and concomitant *in situ* resistometry together with their mass (m_{CuMn}), macroscopic surface area A_{macro} (determined from the outer dimensions of each bulk CuMn sample) and dealloying conditions (electrolyte concentration c_{elec} and applied potential $U_{\text{Ag/AgCl}}$). m_{npCu} denotes the mass of each sample after dealloying and drying, $\Delta m_{\text{exp}}/\Delta m_{\text{theor}}$ is the ratio between the experimentally determined and theoretically calculated mass change, and $\Delta Q_{\text{exp}}/\Delta Q_{\text{theor}}$ is the corresponding charge ratio considering the transferred charge

Sample	m_{CuMn} [mg]	A_{macro} [cm^2]	c_{elec} [M]	U [mV]	m_{npCu} [mg]	$\dfrac{\Delta m_{\text{exp}}}{\Delta m_{\text{theor}}}$	$\dfrac{\Delta Q_{\text{exp}}}{\Delta Q_{\text{theor}}}$
R-1	135.7	1.01	0.1	−300	76.4	0.57	0.8
R-2	127.6	0.78	0.1	−500	72.2	0.58	0.57
R-3	101.1	0.67	0.04	−300	54.5	0.61	0.84
R-F	117.7	0.68	0.1	f.c.	56.4	0.68	—

kink, the resistance change stays constant over the rest of the measurement time.

As visible in the curve of sample R-3 (Fig. 2(b)), no datapoints were recorded between 0.68 h (2440 s) and 1.7 h (6100 s) which is due to an error of the measurement device. However, as the resistance change is very small in this region, it was possible to fit the data in this timeslot with a linear fit (shown in grey).

Fig. 3 shows the relative change in electrical resistance of sample R-F during free corrosion in 0.1 M HCl. The sample was kept in the electrolyte until no change in resistance was observed over several hours (in total 170 h). For comparison, the dealloying curve of sample R-1 is reprinted from Fig. 2. For this sample, the applied potential (-300 mV) was held for 20 h in total. As clearly visible, $\Delta R/R_0$ increases significantly slower during free corrosion and thereby reaches a higher overall value, exceeding that of the potential-controlled sample (R-1) by a factor of 2. Again the three regions, as described above for the potential-controlled dealloyed samples, can be identified.

The determination of the initial resistance R_0 was hampered by fluctuations at the beginning of the measurement. These fluctuations arose from dissolution of Mn, which starts immediately upon immersion even without an applied potential, due to the low standard potential of Mn, which is associated with strong hydrogen bubble formation. Therefore, R_0 was estimated by fitting the resistance increase in a later stage of dealloying (where the recorded data are reasonable stable) by using an exponential function which was then extrapolated towards the start of the measurement ($t = 0$). The value of the exponential function at $t = 0$ is set as R_0, which for all samples is approx. 3–3.5 mΩ.

3.2 Behaviour of fully dealloyed electrodes

For electrochemical characterization of the dealloyed npCu samples, cyclic voltammograms were recorded in 0.1 M KOH and simultaneously the relative change in resistance was measured
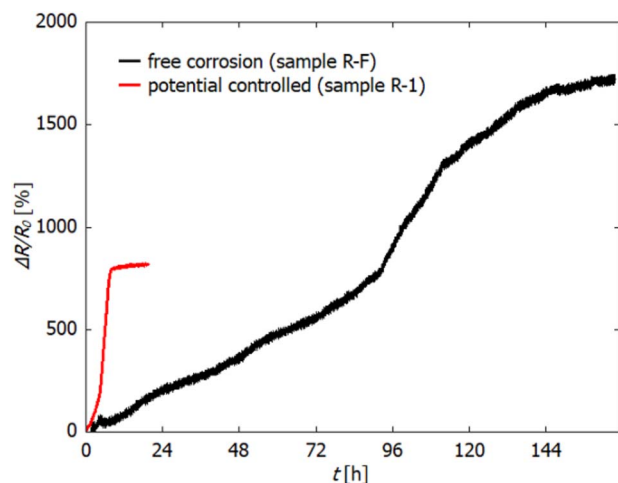

Fig. 3 Relative change in electrical resistance (in %) during free corrosion of sample R-F in 0.1 M HCl (black). For comparison, the resistance change during electrochemically controlled dealloying at -300 mV vs. Ag/AgCl (sample R-1) is reprinted from Fig. 2 (red).

(see Fig. 4(a) and (b)). Again, the current is normalized with respect to the macroscopic surface area (A_{macro} in Table 1).

The open circuit potential (OCP) was in the range of -500 to -600 mV for all freshly dealloyed samples (Fig. 4(a)). The scan was started in the cathodic direction, so that the sample is first reduced before reversing the scan direction and letting (further) electrochemical oxidation of the sample take place (anodic scan). In total, 4.5 cycles are recorded for each sample which means that the measurements are stopped after reduction.

In the $\Delta R/R_0$ vs U scans in Fig. 4(b), R_0 refers to the resistance at the start of each measurement, which is marked by crosses in figure parts (a) and (b). In the first cycle (indicated with dashed lines), no significant change in resistance occurs in the cathodic scan for both samples. This fits the electrochemical data, as no reduction reaction is observed. In the following cycles, a relative resistance increase occurs in the anodic scan at potentials higher than -400 mV. After reversing the scan direction, the resistance increase continues which correlates with the remaining positive current and which, therefore, indicates ongoing oxidation. Under free corrosion (R-F), the relative resistance increase reaches up to 50%. For the potential-controlled sample (R-1), the overall relative change in resistance due to oxidation is significantly lower, only reaching approximately 25%. At approx. -250 mV, the sign of the current becomes negative and reduction sets in. In this potential region, the resistance increase levels off until the resistance starts to decrease at roughly -500 mV. Concomitant with the reduction, the resistance then decreases rapidly.

Although npCu does not exhibit a pure double layer region, charging of a quasi double layer can be examined by recording scan rate dependent CVs in the potential range between -900 and -600 mV (marked by the grey rectangle in Fig. 4(a)).

In Fig. 4 quasi double layer charging (c) with concomitant *in situ* resistometry (d) at varying scan rates between 1 and 5 mV s^{-1} is exemplarily shown for sample R-F. For this specific measurement, the absolute current is plotted as this is relevant for further analysis. For the sake of visibility, only three scan rates, namely 1, 3 and 5 mV s^{-1} are presented. Three cycles were measured for each scan rate, and only the third cycle is shown. In Fig. 4(c), a rectangular-shaped behaviour can be seen as it is characteristic for double layer charging. The dependence of the current on the increasing scan rates arises from the capacitive behaviour of the system.

Fig. 4(d) shows that the resistance change as a function of the applied potential has a linear dependence with a small hysteresis. Additionally, the shift in the course of the consecutive scans at 1, 3, and 5 mV s^{-1} (marked by the dashed arrow) indicates a superimposed continuous decrease of the resistance. This is most likely caused by the slow and continuous reduction of oxide as the quasi double layer lies in the reductive potential regime. It is possibly accompanied by slight coarsening which is a well known phenomenon during electrochemical cycling.[49]

3.3 Scanning electron microscopy

Three different samples were dealloyed in 0.1 M HCl for SEM: one at -300 mV for 20 h (sample M-1), one at -300 mV for 9 h
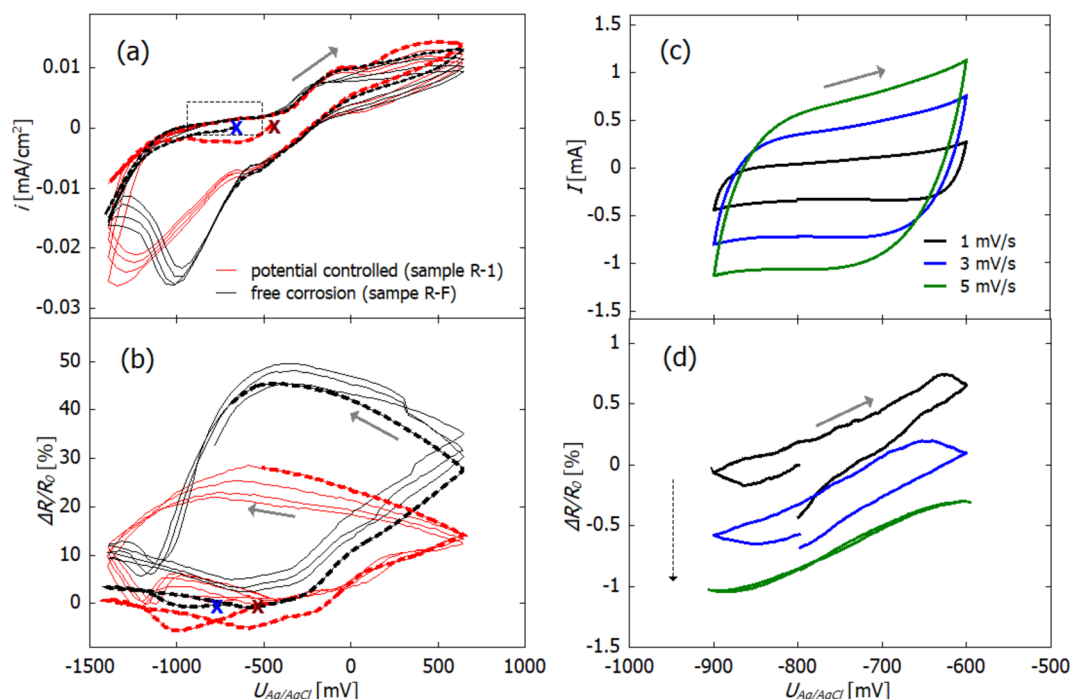
Fig. 4 Cyclic voltammograms (a) and (c) of dealloyed npCu in 0.1 M KOH and concomitant relative change $\Delta R/R_0$ in resistance (b) and (d). (a) and (b) Potential controlled sample R-1 and free corrosion sample R-F; (c) and (d) sample R-F, only. In (a) and (b), the first cycles are indicated by the dashed lines whereby the starting point is marked by red (R-1) and blue crosses (R-F). In (a) and (b) the potential was scanned from −1400 to +350 mV with 5 mV s^{-1}, and in (c) and (d) the potential range is chosen in the quasi double layer region between −900 and −600 mV. The grey rectangle in (a) marks the potential range investigated in (c) and (d). Scans recorded consecutively with 1, 3, and 5 mV s^{-1} are shown in (c) and (d). The grey arrows indicate the scan direction, and the dashed arrow in (d), the order of measurements.

(sample M-2), and one under free corrosion (sample M-F) conditions for 170 h, each followed by cycling in 0.1 M KOH. Sample M-1 was prepared the same way as sample R-1 (see Fig. 3). Dealloying of sample M-2 was cut off directly after the current fell below +5 μA for investigation of the influence of dealloying time (M-2 vs. M-1). Preparation conditions for sample M-F were identical to those for sample R-F.

Fig. 5 shows scanning electron microscopy images from the cross section of the fully dealloyed samples. For each sample an inhomogeneous structure with a clear distinction between two regions is visible. One region is the porous structure with a ligament-morphology characteristic for nanoporous materials (left column S1 to S3) which accounts for the majority of the sample. As the second characteristic region, islands of porous plate-like structures (right column P1 to P3) appear on the sample. An overview of the surface morphology is given in Fig. SI-3 in the ESI.† The SEM images were analysed using the software ImageJ[48] with respect to pore size and the diameter of the platelets. The results are summarized in Table 2 and will be discussed in Section 4.3.

EDS spectra were recorded at several individual points on sample M-1, indicating that on average the porous structure consists of 36 at% O, 24 at% Mn and 40 at% Cu and a plate-like structure of 61 at% O, 32 at% Mn and 6 at% Cu (EDS spectra from the porous structure and from the platelets are shown in Fig. SI-4 in the ESI†). The elemental composition clearly reveals that significant amounts of oxides are present on the surface of

the dealloyed structure. The platelets appear to consist of Mn-oxide.

For more detailed insights into these structures, EDS mapping was performed on overview images of the platelet-rich regions of samples M-2 (dealloyed for 9 h) and M-1 (dealloyed for 20 h). The compositional mapping for Cu, Mn and O is shown in Fig. 6. Clearly, the composition of the platelets changes with dealloying time. For the shorter dealloying time (sample M-2) the platelet-like structures consist of Cu-oxide as well as of Mn-oxide for the sample, whereas for the longer dealloying time (sample M-1) the concentration of Mn-oxide is significantly enriched. XRF analysis was further performed on sample M-1 revealing that the overall ratio between Cu and Mn is 16% to 84%. Oxygen cannot be detected by this method.

4 Discussion

Aiming at an in-depth understanding of nanoporous copper formation by dealloying CuMn, the discussion will start with of the electrochemistry of the dealloying process where the relative change in electrical resistance during dealloying is used to gain information on the temporal evolution of the porous structure (Section 4.1). In Section 4.2, electrochemistry during electrochemical cycling in KOH will be analysed. Finally, in Section 4.3 the findings are compared with SEM images and EDS data to gain insight into the morphology and composition of the porous structure.
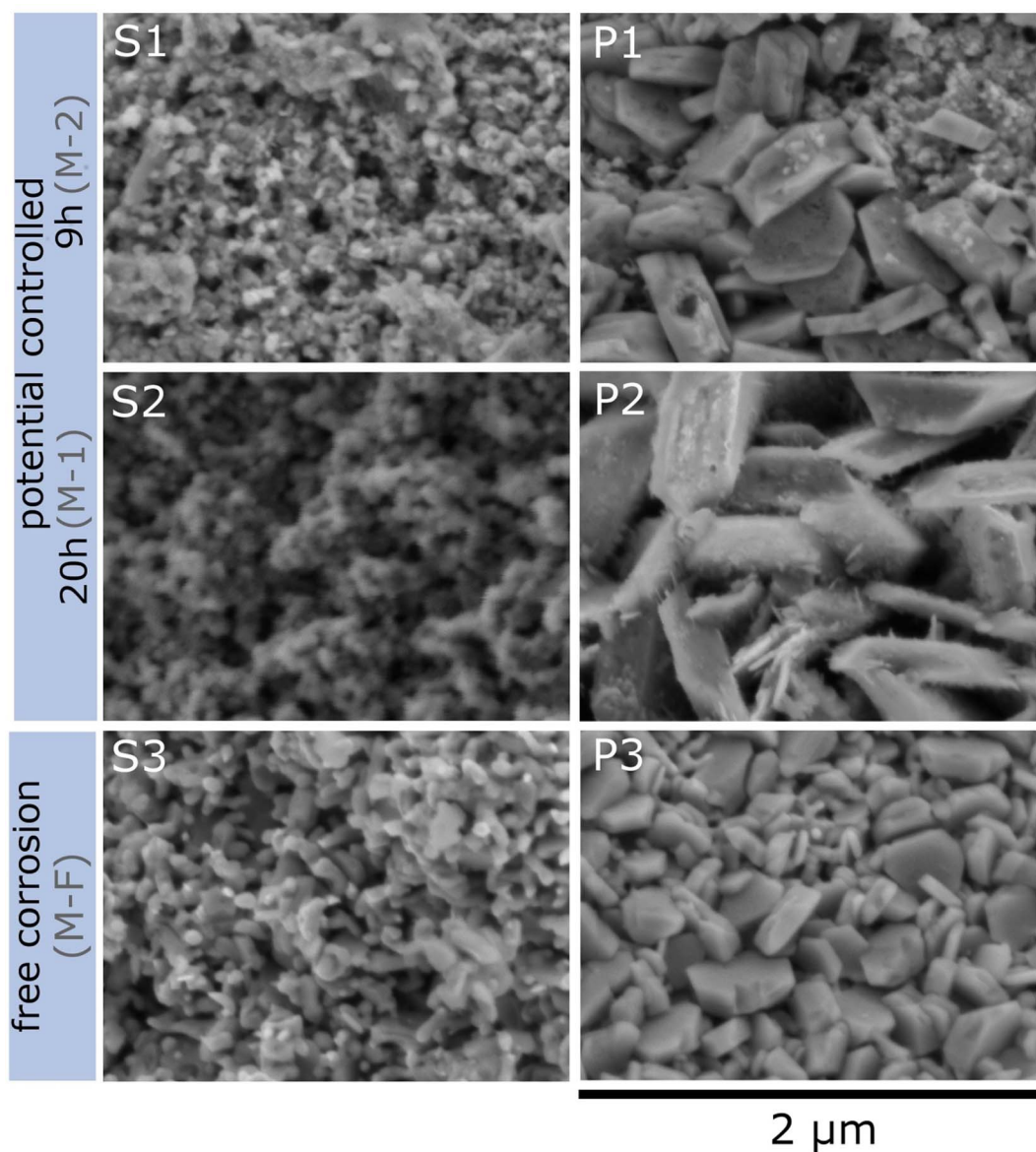
Fig. 5 Scanning electron microscopy (SEM) images of dealloyed npCu. First row: sample M-2 (dealloying time 9 h); second row: sample M-1 (dealloying time 20 h); M-2 and M-1 were both dealloyed at −300 mV. Third row: sample M-F (dealloying time 170 h, free corrosion). The left column shows images taken from the porous structure, and the right column shows the platelets as discussed in the main text.

4.1   Structural evolution during dealloying

For noble metal alloy systems, such as AuAg, PtCu or PdCo, the chemical reactions which result in a faradaic current during dealloying are rather simple. However, because of their high chemical reactivity, the (electro-)chemistry of non-precious alloy systems might be significantly more complex.

Table 2   Structural parameters for sample M-2, M-1 and M-F calculated from SEM images (using ImageJ)

Sample	Platelets [nm]	Pores [nm]
M-2	450	55
M-1	610	66
M-F	280	60

The dealloying of CuMn is performed at pH-values of 1 and 1.4 (0.1 M and 0.04 M HCl, respectively). In this pH regime, according to the Pourbaix-diagrams,[50,51] Cu is stable in its metallic form and Mn dissolves. When immersing CuMn samples in HCl, it can be expected that the etching process starts immediately. Applying a potential more positive than the OCP will further enhance the reaction kinetics. Independent of the dealloying routine (potential controlled or free corrosion), formation of Cu-oxide in acidic electrolytes concomitant to the etching process has been reported (e.g. by Chen et al.[28] and Wang et al.[27]).

Generally, the following (electro-)chemical reactions can be assumed. During free corrosion of Mn in the CuMn alloy, the reaction
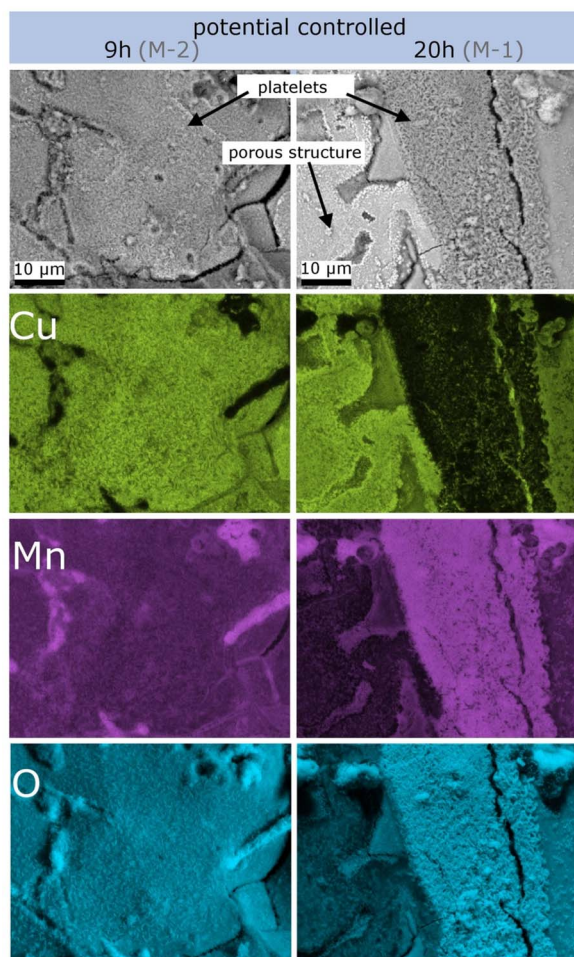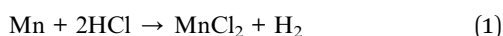
Fig. 6 Elemental analysis of SEM images performed by EDS mapping for Cu, Mn and O in a platelet-rich region. The left column is taken from sample M-2, and the right column, from sample M-1.

$$Mn + 2HCl \rightarrow MnCl_2 + H_2 \qquad (1)$$

will occur spontaneously; Mn is oxidized to Mn^{2+} and Cl is reduced to Cl^- forming a $MnCl_2$-precipitate in the electrolyte and gaseous hydrogen (H_2). The latter is clearly visible by a pronounced formation of gas bubbles on the sample.

If a potential more positive than the OCP is applied, the electrochemically induced reaction

$$Mn \rightarrow Mn^{2+} + 2e^- \qquad (2)$$

occurs additionally which results in the dissolution of Mn. On the counter electrode, the charge is compensated by hydrogen evolution. Subsequently, Mn^{2+} can be further oxidized forming Mn-oxide and thereby can be redeposited on the sample.[52] This reaction is accompanied by evolution of gaseous hydrogen following the reaction

$$Mn^{2+} + 2H_2O \rightarrow MnO_2 + 2H_2. \qquad (3)$$
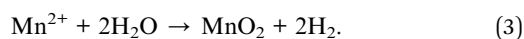
After formation of Mn-oxide, additionally an oxygen reduction reaction catalysed by MnO_2 can occur, which results in a negative current contribution and which is more pronounced at negative applied potentials.[53,54] Oxygen reduction means the conversion of O_2 into OH^- by the consumption of H_2O and electrons. The catalytic process includes several transition states and follows either a two or four electron pathway (hence consuming either two or four electrons during the reductive reaction).[54]

Based on the dissolution and side reactions described above, the present results will be discussed in the following section. During potential controlled dealloying, current *vs.* time is monitored, whereby this charge transfer can only be seen as an effective charge, resulting from all reactions described above. The total charge transferred (ΔQ_{exp}) was determined by integrating the current over time and it was compared to the theoretical charge transfer assuming complete etching of Mn (ΔQ_{theor}) (only considering eqn (2)). The ratio $\Delta Q_{exp}/\Delta Q_{theor}$ is listed for all samples in Table 1 together with the ratio $\Delta m_{exp}/\Delta m_{theor}$ between the mass loss of the dealloyed sample and the theoretical calculated mass loss (again assuming complete etching of Mn according to eqn (2)).

For both ratios a value of one would mean complete etching of Mn, assuming that no side reactions occur. Hence, for $\Delta m_{exp}/\Delta m_{theor}$ a value lower than one ($\Delta m_{exp} < \Delta m_{theor}$) indicates that manganese is still present in the dealloyed structure and/or side reactions occurred which causes a smaller change of m_{exp} compared to the difference Δm_{theor}. Accordingly, for $\Delta Q_{exp}/\Delta Q_{theor}$ a value lower than one could indicate remaining Mn in the structure or an apparent charge decrease (*e.g.* concomitant reduction reactions).

For each sample, $\Delta m_{exp}/\Delta m_{theor}$ is in the range of 0.6, meaning that 60% of the theoretically calculated mass has been etched. Compared to that, $\Delta Q_{exp}/\Delta Q_{theor}$ varies greatly between the samples. It is approx. 80% for R-1 and R-3 and approx. 60% for R-2 (dealloyed at −500 mV). The generally smaller value of $\Delta m_{exp}/\Delta m_{theor}$ compared to that of $\Delta Q_{exp}/\Delta Q_{theor}$ can be explained by the concomitant oxidation reactions giving rise to a reduced mass loss upon etching. Apparently, the charge transfer (ΔQ_{exp}) differs the most from the theoretical value (ΔQ_{theor}) for sample R-2, which is dealloyed at −500 mV. At this more negative potential, the oxygen reduction reaction catalysed by Mn-oxide is more pronounced,[54] as described above. Hence the negative current contribution is larger which presumably causes the deviation of the monitored charge transfer.

As complementary information to analyse the dealloying process, the change $\Delta R/R_0$ in electrical resistance can be used. In addition to the $\Delta R/R_0$–t plots (Fig. 2 and 3), Fig. 7(a) shows $\Delta R/R_0$ as a function of the relative charge transferred Q_{rel} that is obtained by integrating the current *vs.* time curve. In a simple picture, during dealloying the less noble component of a master alloy (in the present case manganese from copper–manganese) is removed and leaves behind a porous skeleton of the more noble metal. Thereby the dealloying front, *i.e.*, the interface between the bulk alloy and porous structure, moves from the surface towards the center of the sample. Surface diffusion of
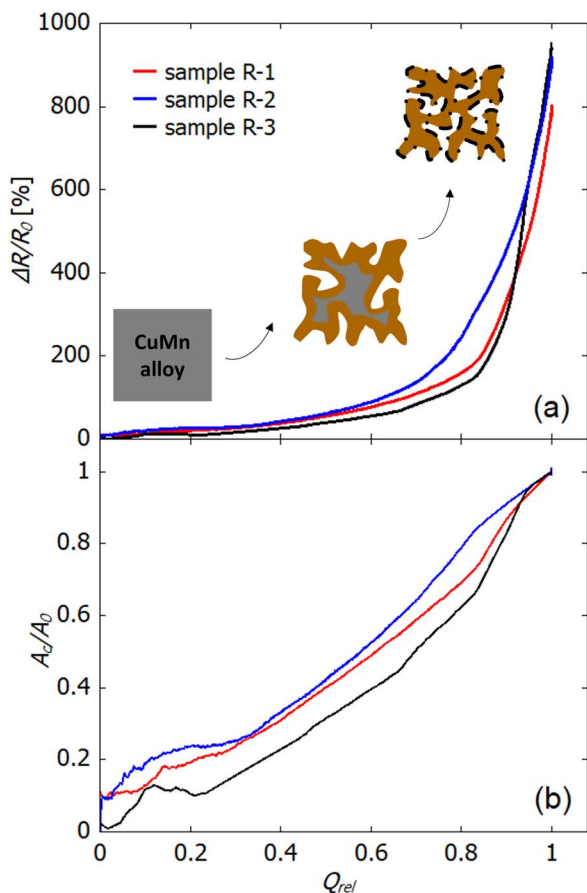
Fig. 7 Analysis of the relative change in electrical resistance during electrochemical controlled dealloying for samples R-1, R-2 and R-3. (a) Relative change in resistance $\Delta R/R_0$ as a function of the relative charge transferred Q_{rel}. The schemes illustrate the formation of the porous structure. Grey represents the initial alloy (CuMn), brown the metallic npCu and black the oxide formed on the surface. (b) Ratio between the converted cross section (A_c) and the total cross section (A_0) of the sample as a function of transferred charge.

the more noble component enables formation of a bi-continuous porous structure. In Fig. 2 (potential-controlled dealloying) and Fig. 3 (free corrosion) as well as in Fig. 7(a) different regimes in $\Delta R/R_0$-evolution can be identified. In the first regime only a slow increase in resistance occurs, which indicates that an alloy backbone is still present. Afterwards, in the $\Delta R/R_0$–Q_{rel} plot above Q_{rel} of approx. 0.85, the resistance increases rapidly which is attributed to a complete consumption of the alloy backbone in the wake of dealloying.

As described above, concomitant to the dissolution process, oxidation takes place. Therefore, the formed oxide contributes to the overall resistance increase. The resistance change arising from pore formation and oxidation cannot be distinguished in a straightforward manner. Nevertheless, some information on the progress of the conversion from the bulk alloy into the porous (oxide-rich) structure is obtained as follows: The measured resistance of the sample can be described as an electrical circuit, consisting of the resistance of the bulk alloy R_m and that of the converted structure R_c

connected in parallel. Furthermore, a relation between the converted cross section (A_c) and the bulk cross section (A_p) is given by

$$\frac{A_c}{A_0} = \frac{\dfrac{1}{R} - \dfrac{1}{R_0}}{\dfrac{1}{\dfrac{\rho_c}{\rho_{fin}}R_{fin}} - \dfrac{1}{R_0}} \tag{4}$$

which only includes the initial electrical resistance of the alloy (R_0), the final resistance of the porous structure (R_{fin}) and the specific resistances of the converted structure ρ_c which evolves over time towards ρ_{fin}. The derivation of eqn (4) is based on the dealloying model presented by Steyskal et al.[43] In this model, it is assumed that behind the etch front the porous structure still evolves significantly, driven by surface diffusion, and hence the specific resistance of the porous structure evolves over time towards ρ_{fin}. However, as can be seen in the SEM images, the pore size and morphology does not change significantly even after prolonged dealloying (M-2 was dealloyed for 9 h and M-1 was dealloyed for 20 h) which indicates that rearrangement of surface atoms is suppressed in the case of CuMn. This most likely results from concomitant oxide formation which reduces the surface diffusivity. Hence, for a simple estimation, a ratio ρ_c/ρ_{fin} of one can be assumed for the entire etching process of CuMn.

With this assumption, the ratio A_c/A_0 can be directly deduced from the resistance data as shown in Fig. 7(b), as a function of the transferred charge Q_{rel}. The ratio A_c/A_0 shows a nearly linear increase over the whole dealloying process when the fluctuations in the early stage up to $Q_{rel} = 0.2$ are not taken into consideration. These fluctuations presumably result from the low resistance value in this regime along with the initial pronounced bubble formation on the sample. When comparing the A_c/A_0–Q_{rel} variation of np-Cu to npAu and npPt, which was studied in a previous work,[43] the characteristics of npCu are more similar to those of npPt than to those of npAu. This is quite noticeable, since in the literature the different porosity evolutions during electrochemical dealloying (and the resulting pore sizes) are typically related to the different melting points,[55] which would connect copper to gold rather than to the high-melting platinum. A lower melting point is associated with a higher surface diffusivity of the remaining atoms, which causes (i) the formation of ligaments with larger diameters at the etch front (bulk dealloying) as well as (ii) stronger rearrangement processes in the already porous structure, leading to further coarsening along with exposure and dissolution of sacrificial element atoms (ligament dealloying). The latter produces a significant charge flow contribution stemming from behind the etch front. While the large pore sizes formed by npCu (bulk dealloying) are well in line with this picture, the low charge flow (ligament dealloying) recorded once the etch front has run through the material, and thus suppressed reordering in the porous structure, cannot be explained via the melting point of copper. In contrast to more-noble element systems, the mechanism blocking surface diffusion behind the etch front

in the case of npCu is the pronounced formation of oxides on the metal surface, which makes a similar evolution of A_c/A_0 for npPt and npCu plausible.

Finally, we compare the electrical resistance variation of R-2 and R-1, and that of of R-3 and R-1 (Fig. 7(a)). For R-1 and R-2 the curves evolve rather similarly, whereby the increase starts earlier for sample R-2 (dealloyed at −500 mV) compared to R-1 (dealloyed at −300 mV). This offset with respect to Q_{rel} is most likely caused by the negative current contribution for sample R-2 associated with the MnO_2-catalysed oxidation at more negative potentials as described above. Comparing R-3 to R-1 (using 0.04 instead of 0.1 M HCl), the increase in relative resistance for R-3 is significantly reduced in the first part, which is also clearly visible in the $\Delta R/R_0$–t representation (Fig. 2). This can most likely be explained by the strong influence of the Cl^- concentration on the surface diffusivity of copper as discussed in the literature.[15] Surface diffusion is highly dependent on the Cl^- concentration in the electrolyte, whereby a higher Cl^- concentration facilitates diffusion. Hence, at lower concentration (as for R-3 compared to R-1) the slower surface diffusion hinders the rearrangement of surface atoms and dealloying kinetics.

4.2 Cu-oxide formation in alkaline electrolyte

The cycling behaviour in 0.1 M KOH (pH 13) after dealloying (Section 3.2) yields additional information on the nanoporous Cu-electrodes. According to the Pourbaix diagrams,[50,51] at this pH Cu is oxidized in an anodic potential scan and reduced at the cathodic potential scan and Mn remains oxidized at any applied potential. In Fig. 4(a) the oxidation/reduction of Cu can be identified with oxidation peaks between −450 and +500 mV (formation of Cu_2O, $2Cu(OH)_2$ and CuO) as well as the corresponding reduction peaks between −450 and −1400 mV, as expected from the literature.[56] The free corrosion sample (R-F) reveals quite similar behaviour to that of the potential-controlled sample. The shift of the reduction peak to more positive potentials might be caused by the different morphologies of the free corrosion sample (see below, Section 4.3).

In the first cycle, no reduction of any primary oxide is visible, which is supported by the rather stable resistance and indicates that any oxide formed during dealloying seems stable over the investigated potential range. This supports the notion discussed above (Section 4.1), that during dealloying, mainly Mn-oxide, rather than Cu-oxide is formed.

Interestingly, during cycling, the peak height decreases from cycle to cycle which is most likely caused (predominantly) by the formation of stable Cu_2O and which thereby reduced the active surface area, as described by Yang et al.[25] and supported by Bai et al.[16] who detected pronounced Cu_2O and CuO formation after multiple cycles. This assumption is also supported by the slight resistance increase from cycle to cycle (Fig. 4(b)).

Obviously, the electrochemically induced resistance variation is significantly higher for the sample (R-F) prepared under free corrosion compared to the potential-controlled sample (R-1) (Fig. 4(b)). As potential-controlled dealloying takes place under stronger oxidizing conditions, more Mn-oxide is formed.

Hence, the tunability of the relative resistance is higher for the free corrosion sample (R-F) as the oxide formation is less pronounced.

The remarkably high resistance variations observed during CV stem from a reversible conversion of copper into low-conducting (hydr-)oxides, leading to an effective decrease of the metallic conductor cross section. Assuming a negligible conductivity of the formed oxide layer, the 30%-increase of $\Delta R/R_0$ corresponds to a decrease of the metallic ligament diameter by about 15% or roughly 10 nm, if the $\Delta R/R_0$-increase is entirely attributed to a corresponding reduction of the conductor cross section. However, to a certain extent, the $\Delta R/R_0$-increase is also due to stronger charge carrier scattering, on the one hand, because of the reduced metallic ligament diameter and, on the other hand, because the charge carrier scattering presumably is stronger at the metal-oxide interface in the oxidized state of the ligaments than at the metal-electrolyte interface of the ligaments in the reduced state.

4.3 Composition and morphology of the porous structure

Finally, the morphology of the porous structure will be discussed in more detail and compared to that in the literature. The SEM and EDS studies (Section 3.3, Fig. 5 and 6, SI-3 in the ESI†) reveal two different morphologies, the porous structure, accounting for the majority of the surface, and in addition platelet-like structures. The latter consists of Cu- and Mn-oxide, where the amount of Mn-oxide increases upon prolonged dealloying (comparison of samples M-2 and M-1, 9 h and 20 h dealloying, respectively; Section 3.3). Cu-oxide arises from post-dealloying cycling in KOH. Similar types of geometric features have been described in the literature before, for dealloyed CuMn. For example, Chen et al.[28] identified nanocube and spheroid nanoparticles after dealloying as Cu_2O. Castillo et al.[32] found that manganese oxide forms nanoplatelets during etching of electrodeposited CuMn which is supported by Biswal et al.[57] who stated that MnO_2 can be electrodeposited from Mn^{2+} in HCl by first oxidation of Mn^{2+} to Mn^{3+}.

The analysis of the SEM-pictures (Table 2) reveal the smallest platelets for the free corrosion sample (M-F). For the potential-controlled sample, the size of the platelets is significantly larger and increases during prolonged dealloying (M-2, 9 h, compared to M-1, 20 h). The smaller platelet size for the free corrosion sample (M-F) is in line with the higher voltage-induced resistance variation (Fig. 4(b)) that has been attributed to the reduced degree of oxidation compared to that for the potential-controlled sample (see Section 4.2).

The pore size lies in the range of 60 nm for all three samples, whereby a slight increase is again observed after prolonged dealloying. In the literature, results on the pore size after dealloying of CuMn in HCl vary greatly, e.g. Hayes et al.[26] reports 130 nm, Chen et al.[28] approx. 20 nm and Tan et al.[35] 70 nm.

From double layer charging (see Fig. 4(c)), the capacitance of the sample can be calculated using a linear fit of the current at a specific potential as a function of scan rate. For the SEM-sample M-1 such type of analysis yields a total capacitance of

0.2 F. Following the analytic expression derived from Detsi *et al.*,[58] an estimation of the pore size d can be carried out based on the total capacitance of the nanoporous sample C and the specific interfacial capacitance of the material investigated (C_{spec}):

$$d = \frac{km}{\rho C} C_{spec} \qquad (5)$$

where m is the mass and k is an empirical parameter (3.7 for disordered nanoporous structures). Assuming that this is pure copper (with a specific interfacial capacitance of 0.02 mF cm^{-2} (ref. 56) and a density[59] of 8.96 g cm^{-3}), this would lead to an average pore size of 30 nm, which is much lower than the value of approx. 60 nm obtained from SEM (see above). However, in eqn (5) it can be seen that a lower density as well as higher C_{spec} (as reported for Mn- and Cu-oxides[60,61]) would result in a larger overall pore size. Hence, this gives additional evidence that the npCu prepared in the present study contains a significant amount of oxides associated with higher specific capacitances.

Eqn (5) can be further used to estimate the specific surface area using the pore sizes deduced from the SEM images. Assuming that the density of the npCu sample is approx. 9 g cm^{-3} (pure copper, see above) or slightly below (taking into account the less dense oxides), a specific surface area of roughly 8 m^2 g^{-1} is obtained for sample M-1. This value lies well in the range of specific surface areas reported for npCu samples with similar pore sizes.[62]

5 Conclusions

The study presented here provides comprehensive insights into oxide formation during dealloying and electrochemical cycling of nanoporous copper in an aqueous electrolyte which is of outmost importance for many fields of application. The synthesis of npCu from a CuMn alloy during free corrosion and potential controlled dealloying in HCl as well as its electrochemical performance in KOH is investigated by *in situ* resistometry. The following structural evolution during formation of nanoporous copper can be proposed. First, etching of Mn and concomitant formation of Mn-oxide in platelet-like structures on the surface takes place. On the surface of these platelets, Mn-oxide is deposited during prolonged dealloying leading to a growth in diameter and an overall enrichment of manganese oxide in these areas. After subsequent cycling in KOH, copper oxide is additionally formed on the surface, resulting in a hybrid composite with a nanoporous copper skeleton decorated with Mn- and Cu-oxide.

While the large observed pore size of the npCu structure is typical for a low-melting metal, a strongly suppressed ligament dealloying is identified in the course of further etching. In contrast to more noble dealloying systems such as npAu or npPt, this can be attributed to the pronounced oxide formation, which blocks rearrangement processes in the porous structure. Reversible oxidation and reduction also enable pronounced resistance variations upon electrochemical cycling in KOH.

As an outlook, the specific control over the materials synthesis described here, and in particular oxide formation, could be of major interest for application in energy storage, sensing and catalysis in the future. Mn and Cu oxide are known from the literature to be perfectly suited for supercapacitors due to their high interfacial capacitance.[5,36] Up to now, great effort has been put into decorated porous samples with Mn-oxides for development of hybrid electrodes for supercapacitors,[63,64] *e.g.* MnO$_2$ and MnO on npAu[5] or npCu[36,65,66] and Cu$_2$O on npCu,[25] always using multi-step preparation routines. The samples in the present study exhibit large amounts of Cu- and Mn-oxides on the internal surface directly after dealloying and electrochemical cycling, which could be enhanced in further studies to maximize the oxide-concentration and hence the interfacial capacitance. Moreover, Cu- and Mn-oxide exhibit great catalytic activities. Together with the large surface area of samples synthesised in the present study, this is very promising for catalytic application, *e.g.* reduction of nitrogen,[13] degradation of methyl orange,[67] oxygen reduction,[53,54] methanol oxidation[25] and reduction of CO$_2$.[14]

Conflicts of interest

There are no conflicts to declare.

Acknowledgements

Notes and references

1 A. Wittstock, J. Biener and M. Bäumer, *Phys. Chem. Chem. Phys.*, 2010, **12**, 12919–12930.

2 K. J. Stine, *Biochem. Insights*, 2017, **10**, 1–12.

3 H. Qiu, H.-T. Xu, L. Liu and Y. Wang, *Nanoscale*, 2015, **7**, 386–400.

4 H.-J. Qiu, Y. Ito and M. W. Chen, *Scr. Mater.*, 2014, **89**, 69–72.

5 X. Lang, A. Hirata, T. Fujita and M. Chen, *Nat. Nanotechnol.*, 2011, **6**, 232–236.

6 J. Biener, A. Wittstock, L. A. Zepeda-Ruiz, M. M. Biener, V. Zielasek, D. Kramer, R. N. Viswanath, J. Weissmüller, M. Bäumer and A. V. Hamza, *Nat. Mater.*, 2009, **8**, 47–51.

7 H.-J. Jin and J. Weissmüller, *Adv. Eng. Mater.*, 2010, **12**, 714–723.

8 S. Shi, J. Markmann and J. Weissmüller, *Electrochim. Acta*, 2018, **285**, 60–69.

9 E. Detsi, M. S. Sellès, P. R. Onck and J. T. M. de Hosson, *Scr. Mater.*, 2013, **69**, 195–198.

10 Y. Chen, H. Feng, Y. Wang, Z. Tang and D. Chua, *Mater. Lett.*, 2018, **226**, 8–12.

11 C. Zhang, Z. Wang, Y. Cui, X. Niu, M. Chen, P. Liang, J. Liu, R. Liu, J. Li and X. He, *Materials*, 2021, **14**, 4348.

12 D. Liu, Z. Yang, P. Wang, F. Li, D. Wang and D. He, *Nanoscale*, 2013, **5**, 1917–1921.

13 Y. Cui, A. Dong, Y. Qu, J. Zhang, M. Zhao, Z. Wang and Q. Jiang, *Chem. Eng. J.*, 2021, **426**, 131843.

14 Y. Peng, T. Wu, L. Sun, J. M. V. Nsanzimana, A. C. Fisher and X. Wang, *ACS Appl. Mater. Interfaces*, 2017, **9**, 32782–32789.

15 Y.-Z. Lee, W.-Y. Zeng and I.-C. Cheng, *Thin Solid Films*, 2020, **699**, 137913.

16 Q. Bai, C. Zhang, F. Tan, F. Wu and Z. Zhang, *Electrochem. Commun.*, 2021, **124**, 106940.

17 E. V. Nikitina, E. A. Karfidov and N. Kazakovtseva, *J. Alloys*, 2020, **845**, 156238.

18 Q. Kong, L. Lian, Y. Liu and J. Zhang, *Micro Nano Lett.*, 2013, **8**, 432–435.

19 Y. Ji, Y. Xing, F. Zhou, X. Li, Y. Chen and L.-H. Shao, *Adv. Eng. Mater.*, 2018, **20**, 1800574.

20 T. Song, M. Yan, Z. Shi, A. Atrens and M. Qian, *Electrochim. Acta*, 2015, **164**, 288–296.

21 X. Yue, R. Hu, J. Qi, J. He, Q. Meng, F. Wei, Y. Ren and Y. Sui, *J. Mater. Eng. Perform.*, 2021, **30**, 1759–1767.

22 N. Wang, Y. Pan and S. Wu, *J. Mater. Sci. Technol.*, 2018, **34**, 1162–1171.

23 C. Yang, Q. B. Zhang, M. Y. Gao, Y. X. Hua and C. Y. Xu, *J. Electrochem. Soc.*, 2016, **163**, D469–D475.

24 Q. Yang, S. Liang, B. Han, J. Wang and R. Mao, *Mater. Lett.*, 2012, **73**, 136–138.

25 Q. Yang, Y. Qin, S. Chu, S. Sun, D. Liu, S. Yang and S. Liang, *Mater. Today Commun.*, 2021, **26**, 101992.

26 J. R. Hayes, A. M. Hodge, J. Biener, A. V. Hamza and K. Sieradzki, *J. Mater. Res.*, 2006, **21**, 2611–2616.

27 L. Wang, H. Xie, J.-C. Shao, H. Yang, P.-Z. Feng and H.-J. Jin, *Scr. Mater.*, 2021, **203**, 114114.

28 L.-Y. Chen, J.-S. Yu, T. Fujita and M.-W. Chen, *Adv. Funct. Mater.*, 2009, **19**, 1221–1226.

29 D. S. Keir and M. J. Pryor, *J. Electrochem. Soc.*, 1980, **127**, 2138–2144.

30 M. J. Pryor and J. C. Fister, *J. Electrochem. Soc.*, 1984, **131**, 1230–1235.

31 U.-S. Min and J. C. Li, *J. Mater. Res.*, 1994, **9**, 2878–2883.

32 E. Castillo and N. Dimitrov, *Electrochem*, 2021, **2**, 520–533.

33 S.-Y. Joo, Y. Choi and H.-C. Shin, *J. Alloys*, 2022, **900**, 163423.

34 S. An, S. Zhang, W. Liu, H. Fang, M. Zhang and Y. Yu, *Corros. Sci.*, 2013, **75**, 256–261.

35 X.-l. Tan, K. Li, G. Niu, Z. Yi, J.-s. Luo, Y. Liu, S.-j. Han, W.-d. Wu and Y.-j. Tang, *J. Cent. South Univ.*, 2012, **19**, 17–21.

36 M. Li, J. Liu, C. Wang, Y. Liu, Y. Sun, C. Qin, Z. Wang, Y. Li, L. Liu and S. Liu, *Chem. Eng. J.*, 2022, **427**, 130861.

37 C. J. Dotzler, B. Ingham, B. N. Illy, K. Wallwork, M. P. Ryan and M. F. Toney, *Adv. Funct. Mater.*, 2011, **21**, 3938–3946.

38 S. S. Welborn and E. Detsi, *Nanoscale Horiz.*, 2020, **5**, 12–24.

39 M. Gößler, E. Hengge, M. Bogar, M. Albu, D. Knez, H. Amenitsch and R. Würschum, *J. Phys. Chem. C*, 2022, **126**, 4037–4047.

40 Y. Zhang, F. Luo, Q. Bai, C. Zhang, B. Yu and Z. Zhang, *J. Phys. Chem. Solids*, 2021, **150**, 109879.

41 F. U. Renner, G. A. Eckstein, L. Lymperakis, A. Dakkouri-Baldauf, M. Rohwerder, J. Neugebauer and M. Stratmann, *Electrochim. Acta*, 2011, **56**, 1694–1700.

42 P. Liu, Q. Chen, Y. Ito, J. Han, S. Chu, X. Wang, K. M. Reddy, S. Song, A. Hirata and M. Chen, *Nano Lett.*, 2020, **20**, 1944–1951.

43 E.-M. Steyskal, M. Seidl, M. Graf and R. Würschum, *Phys. Chem. Chem. Phys.*, 2017, **19**, 29880–29885.

44 E.-M. Steyskal, Z. Qi, P. Pölt, M. Albu, J. Weissmüller and R. Würschum, *Langmuir*, 2016, **32**, 7757–7764.

45 M. Gößler, M. Nachtnebel, H. Schröttner, H. Krenn, E.-M. Steyskal and R. Würschum, *J. Appl. Phys.*, 2020, **128**, 093904.

46 E.-M. Steyskal, M. Seidl, S. Simic and R. Würschum, *Langmuir*, 2018, **34**, 13110–13115.

47 J. Wang, Y. Yang, M. Zhang and S. Yang, *Adv. Funct. Mater.*, 2018, 919–926.

48 C. A. Schneider, W. S. Rasband and K. W. Eliceiri, *Nat. Methods*, 2012, **9**, 671–675.

49 Z. Matharu, P. Daggumati, L. Wang, T. S. Dorofeeva, Z. Li and E. Seker, *ACS Appl. Mater. Interfaces*, 2017, **9**, 12959–12966.

50 B. Beverskog and I. Puigdomenech, *J. Electrochem. Soc.*, 1997, **144**, 3476–3483.

51 W. Sun, D. A. Kitchaev, D. Kramer and G. Ceder, *Nat. Commun.*, 2019, **10**, 573.

52 Z. Rogulski, H. Siwek, I. Paleska and A. Czerwiński, *J. Electroanal. Chem.*, 2003, **543**, 175–185.

53 F. Cheng and J. Chen, *Chem. Soc. Rev.*, 2012, **41**, 2172–2192.

54 J. H. Siow, M. R. Bilad, W. Caesarendra, J. J. Leam, M. A. Bustam, N. S. Sambudi, Y. Wibisono and T. M. I. Mahlia, *Energies*, 2021, **14**, 6385.

55 Q. Chen and K. Sieradzki, *Nat. Mater.*, 2013, **12**, 1102–1106.

56 K. K. Diao, Z. Xiao and Y. Y. Zhao, *Mater. Chem. Phys.*, 2015, **162**, 571–579.

57 A. Biswal, B. Chandra Tripathy, K. Sanjay, T. Subbaiah and M. Minakshi, *RSC Adv.*, 2015, **5**, 58255–58283.

58 E. Detsi, E. de Jong, A. Zinchenko, Z. Vuković, I. Vuković, S. Punzhin, K. Loos, G. ten Brinke, H. A. de Raedt, P. R. Onck and J. de Hosson, *Acta Mater.*, 2011, **59**, 7488–7497.

59 M. Neubronner, T. Bodmer, C. Hübner, P. B. Kempa, E. Tsotsas, A. Eschner, G. Kasparek, F. Ochs, H. Müller-Steinhagen, H. Werner and M. H. Spitzner, D6 Properties of Solids and Solid Materials, in VDI Heat Atlas, SpringerMaterials, 2010, *Copyright 2010* Springer-Verlag, DOI: **10.1007/978-3-540-77877-6_26**.

60 D. P. Dubal, D. S. Dhawale, R. R. Salunkhe, V. S. Jamdade and C. D. Lokhande, *J. Alloys*, 2010, **492**, 26–30.

61 P. Connor, J. Schuch, B. Kaiser and W. Jaegermann, *Z. Phys. Chem.*, 2020, **234**, 979–994.

62 X. Luo, R. Li, Z. Liu, L. Huang, M. Shi, T. Xu and T. Zhang, *Mater. Lett.*, 2012, **76**, 96–99.

63 J. Wei, N. Nagarajan and I. Zhitomirsky, *J. Mater. Process. Technol.*, 2007, **186**, 356–361.

64 J. Kang, A. Hirata, L. Kang, X. Zhang, Y. Hou, L. Chen, C. Li, T. Fujita, K. Akagi and M. Chen, *Angew. Chem.*, 2013, **125**, 1708–1711.

65 T. Jian, J. Zhu, W. Ma, X. Yan, G. Li and J. Zhou, *Appl. Surf. Sci.*, 2020, **529**, 147152.

66 K. Mohamed Racik, A. Manikandan, M. Mahendiran, P. Prabakaran, J. Madhavan and M. Victor Antony Raj, *Phys. E*, 2020, **119**, 114033.

67 T. Kou, C. Jin, C. Zhang, J. Sun and Z. Zhang, *RSC Adv.*, 2012, **2**, 12636.